

Journal of Materials Chemistry C

Accepted Manuscript



This is an *Accepted Manuscript*, which has been through the Royal Society of Chemistry peer review process and has been accepted for publication.

Accepted Manuscripts are published online shortly after acceptance, before technical editing, formatting and proof reading. Using this free service, authors can make their results available to the community, in citable form, before we publish the edited article. We will replace this *Accepted Manuscript* with the edited and formatted *Advance Article* as soon as it is available.

You can find more information about *Accepted Manuscripts* in the [Information for Authors](#).

Please note that technical editing may introduce minor changes to the text and/or graphics, which may alter content. The journal's standard [Terms & Conditions](#) and the [Ethical guidelines](#) still apply. In no event shall the Royal Society of Chemistry be held responsible for any errors or omissions in this *Accepted Manuscript* or any consequences arising from the use of any information it contains.

Flexible thermoelectric materials and device optimization for wearable energy harvesting

Je-Hyeong Bahk^{a1}, Haiyu Fang^b, Kazuaki Yazawa^a, and Ali Shakouri^a

^a Birck Nanotechnology Center, Purdue University, West Lafayette, IN 47907, U.S.A.

^b Materials Research Laboratory, University of California, Santa Barbara, CA 93106, U.S.A.

Abstract

In this paper, we review recent advances in the development of flexible thermoelectric materials and devices for wearable human body-heat energy harvesting applications. We identify various emerging applications such as specialized medical sensors where wearable thermoelectric generators can have advantages over other energy sources. To meet the performance requirements for these applications, we provide detailed design guides regarding the material properties, device dimensions, and gap fillers by performing realistic device simulations with important parasitic losses taken into account. For this, we review recently emerging flexible thermoelectric materials suited for wearable applications, such as polymer-based materials and screen-printed paste-type inorganic materials. A few examples among these materials are selected for thermoelectric device simulations in order to find optimal design parameters for wearable applications. Finally we discuss the feasibility of scalable and cost-effective manufacturing of thermoelectric energy harvesting devices with desired dimensions.

¹ E-mail: bahkjg@uc.edu, currently at Dept. of Mechanical and Materials Engineering, and Dept. of Electrical Engineering and Computer Systems, University of Cincinnati, Cincinnati, OH 45221, U.S.A.

Introduction

Despite the explosive growth of wearable electronics and sensors on the market in recent years, most of the wearable devices are still powered by batteries that are subject to frequent recharging and replacement.[1,2] Often these devices require energy autonomy for an extended service time without the need for the user's intervention. Examples include preventive healthcare for elderly people with wearable medical sensors that monitor the wearer's physiological parameters.[3] These medical sensors need to be preferentially wireless, and operational during the patient's daily activities for a long time up to many years without maintenance or the doctor's direct assistance.

One possible solution for powering these wearable devices without a battery is to harvest energy from human body to generate electricity using a thermoelectric generator. A thermoelectric generator (TEG) is a solid-state device that can convert heat into electricity.[4] When a TEG is attached directly onto the skin, heat from the human body flows through the TEG due to the temperature difference between the skin and the ambient. This heat flow, or the temperature gradient, creates a voltage in the TEG by the Seebeck effect [5], which performs useful work when connected to an external circuit.

Although heat dissipation from a human body largely vary depending on the body location and surrounding conditions, typically heat flow available from the skin under indoor sedentary conditions is $1 \sim 10 \text{ mW/cm}^2$ on the average at $22 \text{ }^\circ\text{C}$ ambient temperature, and a higher heat flow of $10 \sim 20 \text{ mW/cm}^2$ is possible on the wrist, where the heat-carrying radial artery is located near the skin.[6,7] However, the power densities generated by the TEGs made of state-of-the-art Bi_2Te_3 -based inorganic materials have been reported to be less than $60 \text{ } \mu\text{W/cm}^2$ under indoor conditions.[6-11] The limited power densities were mainly due to the low efficiency of the

materials used and the technical difficulties in device manufacturing. Furthermore, the non-flexibility of the inorganic materials and the expensive and non-scalable manufacturing techniques have been major limiting factors for the thermoelectric energy harvesting devices to scale up in size, and increase the power generated.

Hence, there have recently been great interests in synthesizing flexible thermoelectric materials with scalable approaches for wearable energy harvesting applications. A high efficiency thermoelectric material needs to be electrically highly conductive while thermally poorly conductive, as represented in the material figure of merit, $ZT = S^2\sigma T/\kappa$, where S is the Seebeck coefficient, σ is the electrical conductivity, T is the absolute temperature, and κ the is thermal conductivity. The factor $S^2\sigma$ in the numerator is called the power factor. Recently, conjugated polymers have been intensely studied for thermoelectric energy conversion because of their intrinsically low thermal conductivities, easy doping to achieve very high electrical conductivities, as well as their own advantages such as flexibility, material abundance, light-weight, and solution processability.[12,13] Although their ZT values are still lower than those of the inorganic thermoelectric materials ($ZT\sim 1$), there have been significant enhancements in recent years in the thermoelectric performances of organic semiconductors. $ZT = 0.2\sim 0.4$ have been recently reported for poly(3,4-ethylenedioxythiophene) (PEDOT) polymer system.[14,15] Polymer-based nanocomposites with carbon nanotubes[16,17] and inorganic nanostructures[18,19] also showed enhanced power factors. On the other hand, there have been efforts to synthesize paste-type inorganic materials to make them flexible and screen-printable.[20,21]

In this paper, we first review the recent development of wearable thermoelectric generators, and discuss potential applications of these TEGs such as healthcare monitoring. Then we review

recent flexible thermoelectric materials and the physics behind the ZT enhancement in these materials with discussion on charge transport mechanisms. With selected material properties, device simulations are performed to optimize both the output voltage and power with device dimensions and material properties. Finally, we discuss the important recent advances in polymer material deposition and patterning techniques that can be useful for cost-effective and scalable manufacturing of flexible wearable thermoelectric devices.

Devices and applications

Earlier works pioneered by IMEC, Belgium, on the development of thermoelectric energy harvesting devices in the past decade have successfully demonstrated the practicality of hundreds of microwatt-level power generation from human body heat.[6-11,22,23] Their first wearable TEGs were fabricated in 2004 to be equipped on the wrist and serve as a power supply for a low-power wireless sensor.[6] A $\sim 250 \mu\text{W}$ power was generated from the TEG at an ambient temperature $22 \text{ }^\circ\text{C}$, but only a 40 % of the generated power ($100 \mu\text{W}$) was transferred to the sensor node due to the low efficiency of the voltage boost converter. In 2005~2006, watch-sized (6 cm^2 hot side plate with $\sim 10 \text{ cm}^2$ heat sink) TEGs were fabricated to produce $200 \sim 300 \mu\text{W}$ with a output voltage $\sim 1.0 \text{ V}$.[8] The power was increased to $500 \sim 700 \mu\text{W}$ when the wearer walked slowly outdoors due to the forced air convection on a walking person. In these TEGs, thousands of Bi_2Te_3 elements of $200 \times 200 \mu\text{m}^2$ in cross-sectional area were used to create 4-stages of thermoelectric legs with total 7 mm thickness, in order to maintain a sufficiently large temperature gradient across the TEG and a high open-circuit voltage. Also, a relatively bulky fin heat sink was used to enhance the natural air convection heat transfer at the cold side.[8,9]. This

shows how important and difficult keeping a sufficiently large temperature difference across TE elements with an unobtrusive heat sink for a thermoelectric body heat harvester is.

Later, TEGs were used as a wearable power supply for a pulse oximeter on a finger.[24] The TEG generated power ($\sim 100 \mu\text{W}$) enough to operate the pulse oximeter with an measurement update every 15 s, which consumed $\sim 60 \mu\text{W}$. About a half of the consumed power was used for the signal processing, and $\sim 20 \mu\text{W}$ was consumed by two LEDs, and only $3 \mu\text{W}$ for the radio transmission since the signal processing was performed on-board to minimize the amount of data transmitted. A two-channel electroencephalography (EEG) system was powered by TEGs.[25] Since the power consumption was much higher (0.8 mW), total 10 units of TEGs were used to increase the surface area contacting the forehead of the wearer ($\sim 64 \text{ cm}^2$) with 1~1.3 cm thick elements in each. The measured power at 22 °C ambient was about 2.5 mW, resulting in a $30 \mu\text{W}/\text{cm}^2$ power density. Thin, light weight, modular TEGs were integrated in a patient's clothing to perform an electrocardiography (ECG) monitoring.[6] Total fourteen TEGs of $3 \times 4 \text{ cm}^2$ in size and 6.5 mm in thickness each were distributed in an office shirt to generate total 0.8 ~ 1 mW with 1 V load-matching during the wearer's office activities while the ECG system consumed 0.44~ 0.5 mW. Unlike the previous pulse oximeter and EEG system, this ECG system had a secondary battery that was constantly recharged during the operation to compensate the irregular power generation from the distributed TEGs. Later, 16 TEGs of $8 \times 9 \text{ mm}^2$ area and 5 mm thickness each (with a hot plate of 3 cm diameter and a cold plate of $4 \times 3 \text{ cm}^2$ area and 1 mm thickness for each TEG) were integrated in a shirt on the front side of the body, and successfully generated 0.5 ~ 5 mW at ambient temperature of 27 ~ 15 °C, respectively during usual office activities.[11]

If the thermoelectric generator is flexible, so it can be bent, and conformally wrapped onto the curved skin surface, then the TEG may be able to utilize a much larger amount of body heat from the enhanced contact with the skin over a larger surface area to generate more power. In principle, both output power and voltage are proportional to the surface area of a TEG. Increased output voltage can eliminate the necessity of a boost converter. Also, distributed weight over a larger area can enhance user comfort. Fig. 1 shows several types of wearable sensor devices that are powered by flexible thermoelectric energy harvesters. A number of small light-weight medical sensors can be distributed on a patient's body with wireless communications to form a wireless body area network (WBAN).[26,27] These devices are capable of performing health monitoring activities such as EEG, ECG, and other vital signs reading at various locations on the wearer's body.[3] The collected data are transmitted via short-range wireless communication protocols such as Bluetooth, ANT, or Zigbee, and collected by a personal server at a short distance such as a cell phone, which in turn sends out the collected patient's data through the internet or a secure long-distance network to the health service provider for real-time health monitoring. The short-range wireless communication technologies provide efficient, ultra-low power consumption suitable for energy harvesting devices. For example, an experiment showed that Bluetooth Low Energy (BLE) consumes less than 35 μW at 3.3 V supply under 120 s transmission intervals.[28]

The physiological and physical parameters that can be non-invasively monitored by wearable sensors for preventive healthcare include blood pressure[29], respiration rate[30], oxygen saturation (heart rate, pulse oximetry)[24,31], body temperature, and sleep period (actigraphy)[32]. In addition, an adhesive bandage-type wearable sensor for monitoring electrolytes in the wearer's sweat has been recently developed using a battery-free passive radio-

frequency identification (RFID) and paper microfluidics technologies.[33] Hydration, and heat-stress monitoring by sensing electrolytes such as Na^+ and K^+ in sweat are possible with the bandage type device.

Technological advances in integrated circuits, wireless communications, and medical sensors have enabled miniaturized, light weight, ultra-low power, and wearable health monitoring devices. Recently, an ultra-low TEG-powered body sensor node SoC (system on a chip) has been fabricated in a commercial 130 nm CMOS technology for ECG, EEG, and EMG (electromyogram) applications.[34] This SoC integrates low-voltage boost converter, dynamic power management circuits, reconfigurable bio-signal processing units, and RF transmitter in a $2.5 \times 3.3 \text{ mm}^2$ size chip. Only a $19 \mu\text{W}$ power is consumed by the chip for 0.013 % transmission duty cycle with $14 \mu\text{A}$ current at 1.35 V. A commercially available TEG generating $\sim 60 \mu\text{W}$ with 30 mV output voltage was sufficient to power this sensor node without a battery. The low voltage from the TEG was converted up to 1.35 V by an efficient low-voltage boost converter with an efficiency 38 % for the chip operation.[35] This boost converter demonstrates very high up-conversion efficiency greater than 60 % for input voltage as low as 50 mV and input power as low as $10 \mu\text{W}$, thus well suited for low-power energy harvesting devices.

Watkins et al.[36] suggested the use of a TEG with $70 \mu\text{W}$ or higher power for a very small temperature differences of $0.3 \sim 1.5 \text{ }^\circ\text{C}$ in implanted medical devices such as pacemakers and defibrillators to avoid additional surgery needed to replace batteries in these devices. Chandrakasan et al.[37] suggested to scale down supply voltages to 0.5 V or below for micro-power systems utilizing low-power energy harvesting technologies and discussed design challenges for the systems. Mateu et al.[38] generated about 2 mW power using a TEG under

human body heat conditions and designed a power management circuit to power a wireless communication module.

For fabrication of flexible TEGs, Weber et al.[39] sputtered thermoelectric thin films through a shadow mask on a 1.8 m-long flexible polyimide foil substrate to form 900 pairs of transverse TE elements, and coiled up the polyimide stripe to make a coin-size TEG. By rolling up such a long stripe with a large number of TE elements, a voltage higher than 0.8 V was achieved for a small temperature difference like 5 °C in the transverse direction. Kim et al.[20] printed paste-type thermoelectric materials within holes in a polymer fabric using dispenser printing method, and used silver-plated conductive fibers as electrodes connecting TE elements to fabricate highly flexible wearable TEGs. This TEG generated a 178 nW power in ambient temperature of 5 °C when worn on a human chest at 32 °C. More recently, Kim et al.[21] screen-printed paste-type n-type Bi₂Te₃ and p-type Sb₂Te₃ materials (~ 500 μm thick) on a glass fabric to fabricate wearable TEGs. Similarly screen-printed flexible Cu electrodes were bonded onto the TE materials with PDMS elastic polymer as a gap-filling material. A 3 μW power was generated from a small band-shape TEG made up of 11 TE element pairs on human skin at an ambient temperature 15 °C. The power level is expected to scale up with device size.

Flexible thermoelectric materials

Since the early boom of thermoelectrics research in 1950 ~ 1960s for applications in cooling and space missions, advance in thermoelectric materials development had been slow and the state-of-the-art figure of merit ZT had remained around unity until recently because the constituting properties in ZT are mutually coupled, i.e. there is a trade-off between the electrical conductivity and the Seebeck coefficient in most materials.[40] Over the past few decades, nano-

engineering approaches to conventional inorganic thermoelectric materials have enabled great enhancements in ZT . A $ZT \sim 2.2$ at ~ 900 K has been reported recently for the spark plasma sintered Na-doped PbTe:SrTe.[41] The ZT enhancement was attributed to the all-scale hierarchical material structures from nano- to mesoscale that scattered a broad range of phonon mean free paths to significantly reduce the lattice thermal conductivity to $\sim 0.5 \text{ W m}^{-1} \text{ K}^{-1}$. More recently, the single-crystal SnSe has been reported to have a $ZT \sim 2.6$ at 923 K in a crystallographic direction (b -axis) with the ultra-low lattice thermal conductivity in that axis $\sim 0.25 \text{ W m}^{-1} \text{ K}^{-1}$. [42] However, later a theoretical study[43] and experimental results on the polycrystalline SnSe[44,45] showed that the lattice thermal conductivity could be higher than the reported value in Ref. [42], prompting further studies. Skutterudites and clathrates also show high ZT values above unity with inherently low thermal conductivities at mid-temperature range between 600 \sim 900 K.[46,47]

In the low temperature range near room temperature suitable for wearable applications, Bi_2Te_3 -based inorganic materials remain the state-of-the-art thermoelectrics with high ZT values. The nanostructured p-type $\text{Bi}_{0.5}\text{Sb}_{1.5}\text{Te}_3$ showed a $ZT \sim 1.4$ at 100 °C due to the reduced thermal conductivity below $1.0 \text{ W m}^{-1} \text{ K}^{-1}$ by extensive phonon scattering at interfaces, with inherently high power factor on the order of $4,000 \mu\text{W m}^{-1} \text{ K}^{-2}$. [48] For an n-type material, Bi_2Te_3 alloy with Se ($\text{Bi}_2\text{Se}_{0.3}\text{Te}_{2.7}$) showed a $ZT \sim 1.0$ at 125 °C.[49] At room temperature, these ZT values of both the p-type and n-type Bi_2Te_3 alloys slightly decreased to 1.0 and 0.8, respectively, mainly due to the increased lattice thermal conductivities. Previously, the $\text{Bi}_2\text{Te}_3/\text{Sb}_2\text{Te}_3$ superlattices[50] and $\text{PbTe}/\text{PbTeSe}$ nano-dot superlattices[51] were reported to show $ZT \sim 2.4$ and 1.6, respectively, in the cross-plane direction at room temperature, but these values have not been

reproduced to our best knowledge.[52] Furthermore, they were grown by the expensive epitaxial growth techniques that are not scalable to large-scale manufacturing.

All these aforementioned TE materials with high ZT s are inorganic semiconductors, and thus are not flexible nor highly cost-effective to manufacture. Recently, great attention has been attracted to polymer-based thermoelectric materials because of their unique advantages such as mechanical flexibility, light weight, low-cost synthesis, and solution processability. In addition, their thermal conductivities are typically very low due to the highly disordered structures, which is desirable for thermoelectric applications. However, they have typically much lower power factors than those of inorganic TE materials, which has been the main reason that the conjugated polymers have not been thoroughly studied for thermoelectrics thus far. Doping mechanisms, particularly for p-type, have been relatively much studied recently for various applications such as organic solar cells and organic light emitting diodes.[53,54] Electrical conductivities as high as one thousand $S\text{ cm}^{-1}$ or even higher have been easily achieved by oxidizing (p-type) or reducing (n-type) the backbone polymer chains, and maintaining relatively high mobility with high crystallinity or disordered aggregates with sufficiently large molecular weight.[55] Low Seebeck coefficient is the major factor limiting the power factors, and thus ZT of conjugated polymers.

Over the past few years, there have been significant improvements in the thermoelectric figure of merit of conjugated polymer-based materials. Bubnova et al.[14] optimized the oxidation level of poly(3,4-ethylenedioxythiophene) with tosylate (PEDOT:Tos) using a reduction agent to achieve a large power factor $\sim 320\ \mu\text{W m}^{-1}\text{ K}^{-2}$, which is about an order of magnitude greater than that of freshly polymerized PEDOT:Tos, although it is still much lower than those of the state-of-the-art Bi_2Te_3 -based inorganic materials $\sim 4000\ \mu\text{W m}^{-1}\text{ K}^{-2}$. As a result,

$ZT \sim 0.25$ was achieved with the estimated thermal conductivity $\sim 0.37 \text{ W m}^{-1} \text{ K}^{-1}$. In 2013, Kim et al.[15] dedoped p-type PEDOT with polystyrene sulfonate (PSS) in a way to minimize the counter ion volume by partially removing unionized counter ions, which do not contribute to the charge density, but adversely reduce charge carrier mobility. Thus, a very high electrical conductivity $\sim 900 \text{ S cm}^{-1}$ and a reasonably high Seebeck coefficient $\sim 72 \text{ } \mu\text{V K}^{-1}$ were simultaneously achieved to result in a very high power factor $\sim 460 \text{ } \mu\text{W m}^{-1} \text{ K}^{-2}$. Along with the in-plane thermal conductivity $\sim 0.34 \text{ W m}^{-1} \text{ K}^{-1}$, this power factor makes $ZT \sim 0.4$ at room temperature, which is the highest value for organic materials up to date.

However, very recently Weathers et al.[56] found that unlike the results reported in Ref. [15], the electronic thermal conductivity could be significant, even beyond the values predicted by the Wiedemann-Franz relation, in those PEDOT:PSS samples where the electrical conductivity was larger than $\sim 100 \text{ S cm}^{-1}$. As a result, the total thermal conductivity was found to be as high as $1.5 \text{ W m}^{-1} \text{ K}^{-1}$ for the PEDOT:PSS samples that have electrical conductivity $\sim 500 \text{ S cm}^{-1}$. Weather et al.[56] pointed out that the electrical conductivity and the thermal conductivity were measured from two different sets of samples in Ref. [15], which could have resulted in a large uncertainty in the ZT value. Liu et al.[57] independently measured the in-plane thermal conductivity of PEDOT:PSS using time-domain thermoreflectance (TDTR) to find that the anisotropy in thermal conductivity can be very large as 1:0.3 (in-plane:cross-plane) when the electrical conductivity is higher than 500 S cm^{-1} , due to the significant electronic contribution in the in-plane thermal conductivity, qualitatively agreeing with Weather et al.[56]. Typically measurement of in-plane thermal conductivity of organic materials is very difficult because the substrate contribution must be removed. For this, the variable-width 3ω method[58] is usually used as in Kim et al.[15], where two heater lines with a large width contrast are measured to isolate the contribution from

the in-plane thermal conduction. Another method is to remove the substrate and have the thin film suspended between two membranes to directly measure the in-plane thermal conductivity as in Ref. [56]. When the organic film to be measured can be vertically embedded in a template, the TDTR method can be used to measure the in-plane thermal conductivity as in Ref. [57].

Recently, Bubnova et al.[59] reported a very high power factor $\sim 450 \mu\text{W m}^{-1} \text{K}^{-2}$ with the electrical conductivity as high as $1,500 \text{ S cm}^{-1}$ and the Seebeck coefficient $\sim 55 \mu\text{V K}^{-1}$ for PEDOT:Tos. The authors claimed that due to the high crystallinity in this polymer, a bipolaron band was created and overlapped with the valence band to form a semi-metallic band structure, which breaks the trade-off between the electrical conductivity and the Seebeck coefficient, and enhances the two quantities simultaneously. Although further study might be necessary to confirm the detailed band structure with the Fermi level position, bipolar transport effects and so on, it is evident from this paper that the slope of the density of states with respect to the carrier energy around the Fermi level have been increased, which was responsible for the high Seebeck coefficients. On the contrary, they also independently measured PEDOT:PSS with varying doping level, but could not achieve the Seebeck coefficient higher than $\sim 20 \mu\text{V K}^{-1}$ for PEDOT:PSS, in contrast to the high values $> 70 \mu\text{V K}^{-1}$ reported in Ref. [15].

There have been many other reports in recent years on the enhanced power factors for polymer-based materials both p-type and n-type as well as inorganic-based paste-type printable materials. Fig. 2 summarizes the electrical conductivity, Seebeck coefficient, and power factor of the recent key flexible thermoelectric materials. For comparison, the properties of the best bulk Bi_2Te_3 alloys[48,49] are also shown in the figure. Aïch et al.[60] studied a series of p-type poly(2,7-carbazole) derivatives and reported a maximum power factor of $19 \mu\text{W m}^{-1} \text{K}^{-2}$ with electrical conductivity 160 S cm^{-1} and Seebeck coefficient $34 \mu\text{V K}^{-1}$ for PCDTBT. In 2010, the

Yu team reported an enhanced power factor ($\sim 25 \mu\text{W m}^{-1} \text{K}^{-2}$, $\sigma \sim 400 \text{ S cm}^{-1}$, $S \sim 25 \mu\text{V K}^{-1}$) for p-type PEDOT:PSS with carbon nanotubes (CNTs) filling the space between polymer particles to enhance the electrical conductivity.[16] Later the same team further optimized PEDOT:PSS with CNTs and enhanced the power factor to $\sim 160 \mu\text{W m}^{-1} \text{K}^{-2}$ with both enhanced $\sigma \sim 1,000 \text{ S cm}^{-1}$, and $S \sim 40 \mu\text{V K}^{-1}$. [61] Culebras et al.[62] synthesized PEDOT doped with bis(trifluoromethylsulfonyl)imide (BTFMSI) via electrochemical deposition to achieve a maximum power factor $\sim 150 \mu\text{W m}^{-1} \text{K}^{-2}$ ($\sigma \sim 1,100 \text{ S cm}^{-1}$, $S \sim 37 \mu\text{V K}^{-1}$).

In order to enhance the low Seebeck coefficients of organic semiconductors, hybrid nanocomposites with inorganic TE materials have been synthesized. Zhang et al.[63] drop-casted PEDOT:PSS on top of each n-type and p-type Bi_2Te_3 film made of ball-milled nanopowders to achieve enhancements in the effective power factors for both types: $\sim 130 \mu\text{W m}^{-1} \text{K}^{-2}$ ($\sigma \sim 60 \text{ S cm}^{-1}$, $S \sim 150 \mu\text{V K}^{-1}$) for p-type, and $\sim 86 \mu\text{W m}^{-1} \text{K}^{-2}$ ($\sigma \sim 60 \text{ S cm}^{-1}$, $S \sim -120 \mu\text{V K}^{-1}$) for n-type. Although the PEDOT:PSS matrix was p-type, the influence of the n-type Bi_2Te_3 film was significant enough to change the carrier type overall and achieve relatively large magnitudes of n-type Seebeck coefficients. They also tried to stir Bi_2Te_3 nanopowders in PEDOT:PSS solution to disperse the nanoparticles in the polymer matrix, but the film was easily delaminated due to the large hydrophilic surface area of the Bi_2Te_3 particles. Also, it was important to remove native oxide on Bi_2Te_3 particles before the drop-cast by dipping in diluted HCl in order to maintain the high power factor. See et al.[18] synthesized p-type Te nanorods-based nanocrystal films coated with PEDOT:PSS using solution-processing. An average power factor $\sim 50 \mu\text{W m}^{-1} \text{K}^{-2}$ with $\sigma \sim 19 \text{ S cm}^{-1}$, and $S \sim 160 \mu\text{V K}^{-1}$ has been achieved for this hybrid nanocrystal. With the ultra-low thermal conductivity around $0.22 \sim 0.3 \text{ W m}^{-1} \text{K}^{-1}$, a $ZT \sim 0.1$ was achieved. Du et al.[19] incorporated varying contents of exfoliated Bi_2Te_3 nanosheets into PEDOT:PSS to optimize the

power factor up to $\sim 30 \mu\text{W m}^{-1} \text{K}^{-2}$. Recently, Wang et al.[17] reported highly flexible polyaniline (PANI) composites with double-walled carbon nanotubes (DWCNTs) to have a very high optimal power factor $\sim 220 \mu\text{W m}^{-1} \text{K}^{-2}$ with $\sigma \sim 610 \text{ S cm}^{-1}$, and $S \sim 60 \mu\text{V K}^{-1}$ with 30 wt. % DWCNTs. This power factor value was more than two orders of magnitude higher than that of PANI doped with camphorsulfonic acid (CSA) without carbon nanotubes. The mobility of PANI-CSA was greatly enhanced from 0.15 to $7.3 \text{ cm}^2 \text{ V}^{-1} \text{ s}^{-1}$ by about 50 times with the addition of DWCNTs while the carrier concentration was dropped by a factor of four only.

For n-type organic materials, there have been a less, but increasing, number of reports on their thermoelectric properties than p-type materials mainly due to the difficulties in n-type doping of organic semiconductors. In 1993, Wang et al.[64] studied potassium-doped n-type fullerenes K_xC_{70} and found that K_4C_{70} showed $\sigma \sim 550 \text{ S cm}^{-1}$, and $S \sim -22 \mu\text{V K}^{-1}$ at room temperature, which resulted in a power factor $\sim 26 \mu\text{W m}^{-1} \text{K}^{-2}$. Menke et al.[65] reported the maximum power factor of $\sim 12 \mu\text{W m}^{-1} \text{K}^{-2}$ for fullerenes C_{60} doped with $\text{Cr}_2(\text{hpp})_4$. In 2012, Sun et al.[66] investigated both n-type and p-type polymers containing 1,1,2,2-ethenetetrathiolate (ett), poly[$\text{A}_x(\text{M-ett})$], and found that poly[$\text{K}_x(\text{Ni-ett})$] showed the maximum n-type power factor $\sim 60 \mu\text{W m}^{-1} \text{K}^{-2}$ with $\sigma \sim 40 \text{ S cm}^{-1}$, and $S \sim -120 \mu\text{V K}^{-1}$, while poly[$\text{Cu}_x(\text{Cu-ett})$] showed the maximum p-type power factor $\sim 6.5 \mu\text{W m}^{-1} \text{K}^{-2}$ with $\sigma \sim 10 \text{ S cm}^{-1}$, and $S \sim 80 \mu\text{V K}^{-1}$ at room temperature. However these polymers were not solution-processable. Schlitz et al.[67] studied a high-electron mobility, soluble, and air-stable n-type polymer, poly{N,N'-bis(2octyl-dodecyl)-1,4,5,8-naphthalenedicarboximide-2,6-diyl]-alt5,5'-(2,2'-bithiophene)} (P(NDIOD-T2)) doped by dihydro-1H-benzoimidazol-2-yl (N-DBI) derivatives, to find that the electrical conductivity was limited below $10^{-2} \text{ S cm}^{-1}$ by the dopant solubility, while the Seebeck coefficient was as high as $-850 \mu\text{V K}^{-1}$ to achieve the maximum power factor around $0.2\sim 0.6 \mu\text{W m}^{-1} \text{K}^{-2}$. Recently, Kim et

al.[68] reduced the carbon nanotubes films, which were originally p-type after exposed to air, using multiple agents, polyethylenimine (PEI) and diethylenetriamine (DETA), and subsequently using NaBH_4 to make the films n-type. A maximum power factor $\sim 38 \mu\text{W m}^{-1} \text{K}^{-2}$ with $\sigma \sim 52 \text{ S cm}^{-1}$, and $S \sim -86 \mu\text{V K}^{-1}$ was obtained for the reduced CNT films with transport optimization at room temperature. The solution-processed n-type FBDPPV doped with ((4-(1,3-dimethyl-2,3-dihydro-1Hbenzoimidazol-2-yl)phenyl)dimethylamine) (N-DMBI) showed high electron mobility and high doping efficiency to achieve the electrical conductivity $\sim 14 \text{ S cm}^{-1}$, and the power factor $\sim 28 \mu\text{W m}^{-1} \text{K}^{-2}$. [69]

Recently the hybrid superlattices of alternating inorganic TiS_2 monolayers and organic $[(\text{hexylammonium})_x(\text{H}_2\text{O})_y(\text{DMSO})_z]$ layers showed a very high power factor $\sim 450 \mu\text{W m}^{-1} \text{K}^{-2}$ with $\sigma \sim 790 \text{ S cm}^{-1}$, and $S \sim -78 \mu\text{V K}^{-1}$ at room temperature. [70] Extra electrons were injected into TiS_2 layers due to the non-stoichiometry occurred during the single-crystal growth, and stabilized by the intercalated organic cations, providing high conductivity in-plane n-type transport. The in-plane thermal conductivity was also measured to be extremely low $\sim 0.12 \text{ W m}^{-1} \text{K}^{-1}$, so that a $ZT \sim 0.28$ has been achieved at room temperature, which is comparable to those of the best p-type organic semiconductors based on PEDOT.

In addition, there have been efforts to synthesize inorganic materials as paste-type so they can be printed on a flexible substrate while maintaining their high power factors. Kim et al. [20] mixed the Bi_2Te_3 -based powders in a ceramic binder to make both p-type and n-type TE material pastes and printed $500 \mu\text{m}$ thick and 10 mm diameter TE elements on a flexible polyethylene terephthalate (PET) substrate using the dispenser printing method. The B. J. Cho team synthesized both n-type Bi_2Te_3 and p-type Sb_2Te_3 pastes that are screen-printable on a glass fabric. [71,72,21] Element powders in a desired atomic ratio were mixed together with a glass

powder and a binder in solvent in the ball miller for 24 hrs. The glass powder was added to increase adhesion to the glass fabric, and the binder to maintain sufficient viscosity of the pastes. Using these paste-type inorganic materials, both n-type and p-type TE elements of 500 μm thickness were successfully screen printed on a glass fabric to fabricate highly flexible and light-weight ($\sim 0.13 \text{ g cm}^{-2}$) TEGs for wearable applications.[21] The printed n-type Bi_2Te_3 paste showed a power factor $\sim 1,200 \mu\text{W m}^{-1} \text{K}^{-2}$ with $\sigma \sim 600 \text{ S cm}^{-1}$, and $S \sim -140 \mu\text{V K}^{-1}$, and the p-type Sb_2Te_3 showed a similar power factor $\sim 1,200 \mu\text{W m}^{-1} \text{K}^{-2}$ with $\sigma \sim 1300 \text{ S cm}^{-1}$, and $S \sim 95 \mu\text{V K}^{-1}$. These power factors are lower than those of the bulk-grown inorganic counterparts by a factor of 3~4, but still much higher than those of the best polymer-based TE materials discussed earlier as shown in Fig. 2. The thermal conductivities were measured to be 1.0 and 1.3 $\text{W m}^{-1} \text{K}^{-1}$ for the n-type and p-type pastes, respectively, which resulted in $ZT \sim 0.3$ for both materials.

Device optimization

Fig. 3 shows a schematic of a thermoelectric energy harvester made of multiple n-type and p-type elements, and the thermal and electric circuit models used for device simulation. Total N pairs of n- and p-type elements are connected electrically in series, so that the voltages induced in each element are all added up to apply a sufficiently large voltage to the load (external circuit). Since the temperature inside the body ($\sim 37 \text{ }^\circ\text{C}$) is higher than the ambient temperature ($\sim 22 \text{ }^\circ\text{C}$), heat Q flows by conduction from inside the body, through the skin to the top side of the TEG, where the TEG hot-side substrate is in contact with the skin, and then through the TEG to the bottom, where a heat sink dissipates the remaining heat to the ambient. When it flows through the TEG, the heat is converted into electricity to do useful work at the load. The ratio between

the work done at the load divided by the heat input Q is the efficiency of the TEG, which is typically 0.1 ~ 0.5 % for a good TEG made of the state-of-the-art materials.

One can optimize the power and voltage output of a TEG for given material properties and environmental conditions by adequately designing the TE element dimensions, i.e. the cross-sectional area, thickness, and the fill factor F ($0 < F < 1$), which is the fractional area coverage of the TE element. According to Yazawa et al.[73], a smaller fill factor lower the optimum thickness for maximum power output. The odd fraction $(1-F)$ inside the TEG module that are not covered by TE elements needs to be filled with another material called the gap filler for mechanical support and material encapsulation, especially when the fill factor is very small ($\ll 1$). There can be radiative thermal cross talk between the interim walls of the hot and cold side substrates, as well as conductive heat transport across the air gap if the space is not filled.[74] Since heat still can flow through the gap filler from hot side to cold as modeled as a parallel thermal resistance ψ_{filler} in the thermal circuit model in Fig. 3(b), the gap filler must be a good thermal insulator to minimize the parasitic conduction heat loss. Silica aerogel is an excellent candidate for a gap-filler material, having extremely low thermal conductivity close to that of air ($\sim 0.03 \text{ W m}^{-1} \text{ K}^{-1}$) and light weight, castable into a wide range of sizes, and capable of suppressing convection with its porous structure.[75]

In steady-state, all the heat input and output are balanced off at each node of the thermal circuit, i.e. at the two ends of a TE element as shown in Fig. 3(b). When a TEG operates and generates electricity allowing electric current to flow through the circuit, Joule heating occurs inside the TE elements, at the contacts between TE elements and electrodes due to the finite contact resistance, as well as inside the electrodes. The Joule heating contribution from electrodes is typically much less than the Joule heating in the TE elements.[76] Also, we

assumed the contact resistance on the order of $10^{-5} \sim 10^{-6}$ Ohm cm^2 , which also turns out to be much smaller than the resistances of TE elements for the cross-sectional areas used in the simulations. The Joule heating occurring inside a TE element is divided equally to the both directions of the TE element, i.e. $Q_{J,c} = Q_{J,h} = \frac{1}{2}(I^2R)$ in Fig. 3(b), where R is the electrical resistance of the TE element, and I is the current. This discrete weighting of the volume heating exactly matches the fully distributed modeling as far as the condition is steady state and the material of the TE element is uniform.

In addition, Peltier effect occurs at each node, either cooling or heating the junction depending on the current direction, i.e. $Q_P = \Delta S I$, where ΔS is the Seebeck coefficient difference between the TE element and the electrode making junction at the node, T is the temperature at the node. During power generation, the hot side end of a TE element is always cooled by the Peltier effect, while the other cold end is heated. Hence, these Peltier effects slightly reduce the temperature difference across the TE element. Usually these terminal effects are small because the heat conduction is dominant over the Peltier and Joule terms at the maximum power output condition. Nonetheless, these Peltier and Joule terms create coupling between the thermal circuit and the electric circuit, so the two circuits must be solved simultaneously to find the temperatures at the nodes and the current I . Due to the coupling, it is important to co-optimize the thermal and electrical impedances of the system to achieve maximum power output.[73] At the optimal design, ΔT applied across the TE elements becomes approximately a half of the total $\Delta T_{\text{total}} (= T_s - T_a)$ for smaller ZT materials, i.e. $ZT < 1$.

The TE device simulation tool used in this paper has been published online at nanohub.org for public use.[77] This simulation tool is capable of simulating a TEG system with temperature-dependent TE material properties, which involves iterative one-dimensional finite element

simulations to numerically solve for the temperature profile across TE elements. In wearable applications, however, the temperature difference applied to TE elements is small, only a few degrees, so that the assumption of temperature-independent material properties is still reasonable. On the other hand, temperature-dependency of material properties must be taken into account in general cases of waste heat recovery applications, where a large temperature difference, 100 ~ 200 °C or even larger, can be commonly applied across the TE elements.

There have been several reports about the thermal resistance per unit area of human body on various body locations.[7, 11, 78, 79] Basically body thermal resistance varies widely depending on the location on the body. For example, one of the lowest thermal resistance is measured on the radial artery on the wrist to be $\sim 150 \text{ cm}^2 \text{ K W}^{-1}$, and it is much higher to be $\sim 300 \text{ cm}^2 \text{ K W}^{-1}$ on the anterior leg. In addition, these thermal resistance values are a function of heat flux on the location, decreasing with increasing heat flux[11], which means that when a TEG is equipped on that body location, the body thermal resistance reduces because the TEG enhances heat conduction on the skin. About $60 \text{ cm}^2 \text{ K W}^{-1}$ has been measured on the radial artery when a TEG was worn on it with heat flow above 100 mW cm^{-2} . [11] However, if the heat flow is higher than $25 \sim 30 \text{ mW cm}^{-2}$, the wearer would feel sensation of coldness, which would cause discomfort when worn for a long time.[9] In our simulations, we assume relatively low heat flow with our TEGs to simulate, and thus conservatively choose the value for the average body thermal resistance around the wrist to be $200 \text{ cm}^2 \text{ K W}^{-1}$, which includes the interface thermal resistance between the skin and the TEG, i.e. $\psi_{\text{skin}} + \psi_{\text{interf}}$.

At the cold side, we chose the heat sink thermal resistance to be $\psi_{\text{sink}} = 1,000 \text{ cm}^2 \text{ K W}^{-1}$. Note that in Ref. [8], a large-area ($\sim 12 \text{ cm}^2$), and obtrusive fin-type metallic heat sink was attached at the cold side to enhance the heat conduction, and its thermal resistance was estimated

to be $\sim 700 \text{ cm}^2 \text{ K W}^{-1}$. It will be a challenge to develop a flexible, light-weight, and unobtrusive heat sink having a comparable or smaller thermal resistance than this value for flexible devices. It is important to keep the heat sink thermal resistance as low as possible (as far as it does not cause severe sensation of coldness) for two reasons: first, it increases the heat input coming through the TEG by reducing the total thermal resistance of the device for a fixed total temperature difference available, $(T_s - T_a)$, which in turn increases the power output. Second, it reduces the thickness of TE elements to keep ΔT across the TE elements at optimal $\sim \frac{1}{2}(T_s - T_a)$, which can reduce the material cost as well as the manufacturing cost.

To understand the impact of the material properties, we used two representative sets of material properties in our simulations as shown in Table 1: the first one represents low electrical conductivity, high Seebeck coefficient, and low thermal conductivity material. The electrical conductivity and Seebeck coefficient values were excerpted from Zhang et al.[63], properties for the PEDOT:PSS polymer coated on an inorganic Bi_2Te_3 film, while the thermal conductivity is set to $0.3 \text{ W m}^{-1} \text{ K}^{-1}$, a typical value for highly disordered conjugated polymers. We call this imaginary material “Inorganic-polymer hybrid”. In fact, the power factor and the resulting ZT value for this material are much lower than those already reported for highly conductive PEDOT-based polymers. However, we wanted to keep the electrical conductivity below 100 S cm^{-1} since the recent papers showing the carefully measured in-plane thermal conductivities[56,57] pointed out that the electronic contribution to thermal conductivity could be significant for such a highly conductive polymer. The second set of material represents high electrical conductivity, reduced Seebeck coefficient, and high thermal conductivity. All the properties for the second set were excerpted from Kim et al.[21], properties for the screen-printed paste-type Bi_2Te_3 and Sb_2Te_3 materials. We call this “Screen-printed inorganic”.

We performed device simulations with these two materials. A wrist-band type device of 3 cm width and 15 cm length to cover an average adult wrist perimeter was selected for the simulation, and the cross-sectional area of each TE element was fixed to be $0.5 \times 0.5 \text{ mm}^2$. Note that a much larger cross-sectional area may not achieve sufficient power output because ΔT across the TE elements would be too small due to the small thermal resistance of TE elements with such a large cross-section. The fill factor F is an independent variable, from which total number of TE element pairs was determined as $F \times (\text{total module size}) / (2 \times (\text{each element size}))$. The thickness of TE elements was also varied as another independent variable. The thermal conductivity of the gap filler was initially set to $0.03 \text{ W m}^{-1} \text{ K}^{-1}$ and varied later to investigate its effect on power output. For each calculation, we matched the load resistance to the total electrical resistance of the TEG for maximum power output.

Fig. 4 shows the calculated voltage and power output from the wrist-band TEGs as a function of TE element thickness for several different fill factors. Overall, the power output from the inorganic-polymer hybrid TEG is lower than that from the screen-printed inorganic TEG because of its lower ZT (Table 1), but higher voltage output is achieved because of its higher Seebeck coefficient and its lower thermal conductivity, which created a larger ΔT for a similar thickness. As shown in Fig. 4(b), TE elements thicker than 4~5 mm are needed to obtain power output greater than $100 \text{ }\mu\text{W}$ for the wrist-band TEG made of the inorganic-polymer hybrid material, while only 1 ~ 2 mm thickness is needed for the screen-printed inorganic material because of its higher ZT . However, the screen-printed inorganic may need a boost converter to achieve sufficiently high voltages of 1 ~ 3 V. This could be overcome if a larger size of TEG is used because both the voltage and power output are proportional to the module size.

Different behaviors of the two materials with fill factor states an important design strategy. As one can see in Fig. 3(b), higher fill factors (0.3 and 0.5) produce larger power than lower fill factors for the hybrid material. This is because when the fill factor become small, the parasitic heat conduction through the gap filler becomes significant, which reduces the power output. Since the thermal conductivity of the hybrid TE material was $0.3 \text{ W m}^{-1} \text{ K}^{-1}$, ten times higher than that of the gap filler ($0.03 \text{ W m}^{-1} \text{ K}^{-1}$), when the fill factor is 0.1, meaning that only 10 % of the total area is covered by the TE elements, while 90 % is covered by the gap filler, then the thermal conductances of the two parallel thermal paths become comparable with each other, so a half of the heat energy is just lost by flowing through the gap filler. Therefore, the power output is cut to about a half. When the fill factor is sufficiently large, the heat loss through the gap filler becomes negligible, so that a larger power can be produced. On the other hand, since the printed inorganic material has much larger thermal conductivity than that of the gap filler, most of the heat flows through the TE elements, and the heat loss through the gap filler is very small even for very small fill factors like 0.05 as shown in Fig. 4(d). Therefore, the smaller the fill factor, the larger the power output for the printed inorganic material, due to the increased temperature difference across the TE elements with increased thermal resistances. Note that there is a trade-off between the voltage output and power output for the printed inorganic because a smaller fill factor reduces the total number of TE elements for a fixed module size, and total voltage output is proportional to the number of TE elements. In contrast, both voltage and power outputs were higher with a larger fill factor for the hybrid material due to the reduced heat loss through the gap filler.

We performed additional simulations with varying gap filler thermal conductivity to see its impact on the power output of the hybrid material. As shown in Fig. 5, significant drop of power

output is observed when the gap filler thermal conductivity increases up to $0.1 \text{ W m}^{-1} \text{ K}^{-1}$ compared to the case with no gap filler conduction assumed. This effect will be more apparent when the fill factor is smaller. From this observation, it is fair to say that having relatively high thermal conductivity for the TE material ($\sim 1 \text{ W m}^{-1} \text{ K}^{-1}$ should be reasonably good) and keeping the thermal conductivity of gap filler very low is desirable to minimize the heat loss through the filler. But to keep the power output high at the same time, a high ZT value is necessary, meaning that a high power factor is crucial. On another thought, as long as the heat loss through gap filler can be kept small, a reasonably low thermal conductivity may provide an opportunity to reduce the thickness of TEG elements, which is desirable for cost-effective generators with reduced material cost.[80,81]. Thinner materials tend to be more flexible in general, so further preferable in flexible electronics.

Fabrication and deposition methods

As discussed in the previous sections, fabricating flexible TEGs, especially those capable of producing significant power on the order of hundreds μW , is of vital importance. To realize the flexibility of a TEG, soft materials such as organics, hybrid composites, and paste-type materials, are preferred to rigid inorganics. In addition, solution-processability is a key to scalable and cost-effective fabrication of TEGs. In this section, we review the techniques used to fabricate flexible thermoelectric devices, summarize the performance of the devices reported in literature and discuss the potential challenges.

The techniques applied to fabricate flexible thermoelectric devices in literature include screen printing[21, 82-89], inkjet printing[20,90-95], molding[96,97], and lithography[14,98]. Screen printing is the most commonly used method due to its straightforward process, which

involves casting ink onto a flexible substrate covered by a pre-patterned mask.[86] The potential of screen printing can be magnified when coupled with the roll-to-roll (R2R) process that is capable of continuously manufacturing meter-long modules. Søndergaard et al.[83] developed an automatic R2R process and screen printed as many as 18,000 TE elements composed of PEDOT:PSS and Ag paste with an active area of $1 \times 6 \text{ cm}^2$ for each pair of elements. Another interesting technique is inkjet printing, where the original ink cartridge is replaced by the thermoelectric material formulation, which is later dispensed onto substrates following the patterns preset by a controlling computer.[99] The advantages of inkjet printing include minimal human labor requirement, high precision dispensing and little material waste. Madan et al.[93-95] developed an epoxy embedded with percolated Sb_2Te_3 (p-type) or Bi_2Te_3 (n-type) particles, which is then printed onto flexible substrates to form tens of element pairs with planar and circular patterns. Although printing is convenient and fast to create complex patterns, most applications are limited to use temperature gradient in the in-plane direction due to the micrometer thicknesses of the printed films. For wearable energy harvesting, TEGs that take advantage of temperature gradient in the cross-plane direction are suitable. Molding and lithography provide solutions to this problem. Jo et al.[96] and Sheng et al.[97] molded PDMS membranes with arrays of cavities, which are then filled with thermoelectric materials whose thicknesses reach millimeters, enough to maintain a significant temperature difference in the cross-plane direction. Bubnova et al.[14] applied the photolithography technique to create cavities in a photoresist SU-850, and then used the inkjet printing technique to dispense materials into the cavities, which potentiates the large-scale manufacturing. Besides the techniques reviewed above, there are also some efforts using free standing carbon nanotube composite films that can be easily cut into many pieces with scissors and each piece can be used as a TE element

in a large TEG.[68,100,101] For example, Kim et al.[68] made a TEG composed of stacks of 72 pieces of CNT composite films with this method. Additionally, it is worth noting that a handful of papers also demonstrated the potential of vacuum deposition of pure inorganic thin films with micrometer thicknesses to make flexible thermoelectric modules.[102-104]

Table 2 summarizes the materials and performance of flexible TEGs reported in literature. Intriguingly, around 60% of the TEGs have power output larger than 1 μW with a temperature difference of 100 K or less, some of which are enough to power a wireless sensor[94], electrochromic sensor[68], LED[86] and even a calculator[97]. Some of the TEGs reached microwatt-scale power output even at a small temperature difference of 20 K.[93,94] In Table 2, the highest power output is 1 mW with an open circuit voltage of 1.5 V achieved in a TEG made of 220 pairs of ethylenetetrathiolate (ett)-based organic TE elements.[97]

Herein, we observe some trade-offs and challenges for TEG fabrication based on the data summarized in Table 2. First, a TEG with a larger N tends to produce better performance. It can be understood through the formula of the open circuit voltage ($V_{oc} = N(|S_p|+|S_n|)\Delta T$) and the maximum power output ($P_{max} = N(|S_p|+|S_n|)^2\Delta T^2/(4r_{in})$), where r_{in} is the resistance of a TE element pair, that increasing N will improve the device performance for a fixed ΔT . Aforementioned methods have good scalability and over 100 element pairs were fabricated through screen printing [83,86,88] and molding [97] without any additional technological breakthrough. A parameter that has not been taken into account is the internal electrical resistance of the TEG, which includes the intrinsic resistance of thermoelectric elements as well as the parasitic contact resistances and the series resistances from the electrodes. Although some TEGs can produce reasonable open circuit voltage, the large internal resistance leads to a small working current, which limits the power output. For instance, the TEGs with internal resistance

larger than 2 k Ω in Table 2 have relatively small power outputs, some of which are even under 1 μ W.[68,98,100,104] Making thicker films by printing multiple times or optimizing geometrical ratio between p- and n-type elements[85] can help reduce the resistance of thermoelectric elements while the contact resistance can be minimized by evaporating good ohmic contact layer between TE elements and electrodes. For example, Kim et al.[21] deposited Ni between Bi₂Te₃/Sb₂Te₃ epoxy and copper electrodes and achieved an internal resistance less than 1 Ω . Furthermore, a poor thermal interface between the thermoelectric elements and the thermal contacts can also reduce the performance by restricting the apparent temperature difference across the thermoelectric elements. For example, the module composed of hundreds of PEDOT:PSS/Ag junctions made by Søndergaard et al.[83] had an unusually small open circuit voltage (0.18 mV at a temperature difference of 65 K in the cross-plane direction), which is due to the major temperature drop occurred in the 60 μ m thick substrate instead of the 1.3 μ m thick PEDOT:PSS active layer. The most common material Bi₂Te₃ and Sb₂Te₃ are found to be compromised with insulating epoxy for flexibility. The material often needs high temperature (250 – 350 °C) annealing, which may require a high process cost. Development of new high *ZT* organic materials with low temperature scalable processes still remains a major challenge.

Conclusions

In this paper, we reviewed the recent advances in the flexible thermoelectric materials and devices development for wearable energy harvesting applications. We identified various applications in health monitoring for thermoelectric energy harvesters. Organic materials have shown great potentials to be excellent thermoelectric materials for these applications with their own advantages in addition to very low thermal conductivity, i.e. flexibility, light weight,

material abundance, and low-cost manufacturing. Recently their thermoelectric figures of merit have shown significant enhancement due to the advances in doping control, material synthesis and processing techniques. Inorganic based flexible and printable materials have been also developed with high ZTs . For sufficient power generation above $100 \mu\text{W}$, a mm-level thickness of TE materials and a large device size are required. Optimization with fill factor and gap filler material is also essential. Finally, scalable additive manufacturing such as screen printing, inkjet printing, and molding have shown promising results for future low-cost, high performance flexible TEG fabrication. Yet, further technological advances in cost-effective manufacturing of flexible TE materials and devices will be necessary to realize the first commercially available wearable thermoelectric energy harvesters.

References

- (1) J. Hsu, “Printed, flexible, and organic wearable sensors worth \$244 millions in 10 years,” in *IEEE Spectrum*, Sept. 29, 2014.
- (2) M. Stoppa, and A. Chiolerio, *Sensors*, 2014, **14**, 11957-11992.
- (3) S. Patel, H. Park, P. Bonato, L. Chan, and M. Rodgers, *J. Neuroeng. Rehabil.* 2012, **9**, 21.
- (4) G. J. Snyder, “Small Thermoelectric Generators” *Interface*, Fall 2008, p. 54.
- (5) D. M. Rowe, ed. *Thermoelectric Handbook: Macro to Nano* (CRC Press, Boca Raton, 2005).
- (6) V. Leonov, in *Wearable Monitoring Systems*, edited by D. D. Rossi (Springer, New York, 2010), Chap. 2, pp. 27-49.
- (7) V. Leonov, *ISRN Renewable Energy*, 2011, 785380. (doi:10.5402/2011/785380)
- (8) V. Leonov, T. Torfs, P. Fiorini, and C. V. Hoof, *IEEE Sensors J.*, 2007, **7**, 650-657.
- (9) V. Leonov and R. J. M. Vullers, *J. Electron. Mater.*, 2009, **38**, 1491-1498.
- (10) Z. Wang, V. Leonov, P. Fiorini, and C. V. Hoof, *Sensors and Actuators A*, 2009, **156**, 95-102.
- (11) V. Leonov, *IEEE Sensors J.*, 2013, **13**, 2284 – 2291.
- (12) O. Bubnova and X. Crispin, *Energy Environ. Sci.*, 2012, **5**, 9345–9362.
- (13) Y. Chen, Y. Zhao, and Z. Liang, *Energy Environ. Sci.* 2015, **8**, 401-422.
- (14) O. Bubnova, Z. U. Khan, A. Malti, S. Braun, M. Fahlman, M. Berggren, and X. Crispin, *Nat. Mater.*, 2011, **10**, 429-433.
- (15) G.-H. Kim, L. Shao, K. Zhang and K. P. Pipe, *Nat. Mater.*, 2013, **12**, 719–723.
- (16) D. Kim, Y. Kim, K. Choi, J. C. Grunlan and C. Yu, *ACS Nano*, 2010, **4**, 513–523.
- (17) H. Wang, S.-I. Yi, X. Pu, and C. Yu, *ACS Appl. Mater. Interfaces*, 2015, **7**, 9589-9597.

- (18) K. C. See, J. P. Feser, C. E. Chen, A. Majumdar, J. J. Urban, and R. A. Segalman, *Nano Lett.*, 2010, **10**, 4664-4667.
- (19) Y. Du, K. F. Cai, S. Chen, P. Cizek, and T. Lin, *ACS Appl. Mater. Interfaces*, 2014, **6**, 5735–5743.
- (20) M. K. Kim, M. S. Kim, S. E. Jo, H. L. Kim, S. M. Lee, and Y. J. Kim, Proc. 17th Int. Conf. Transducers & Eurosensors, 2013, p. 1376-1379. (10.1109/Transducers.2013.6627034)
- (21) S. J. Kim, J. H. We, and B. J. Cho, *Energy Environ. Sci.*, 2014, **7**, 1959-1965.
- (22) R. J. M. Vullers, R. van Schaijk, I. Doms, C. Van Hoof, and R. Mertens, *Solid-State Electron.*, 2009, **53**, 684-693.
- (23) V. Leonov, and R. J. M. Vullers, *J. Renewable Sustainable Energy*, 2009, **1**, 062701.
- (24) T. Torfs, V. Leonov, and R. J. M. Vullers, *Sens. Transducers J.*, 2007, **80**, 1230-1238.
- (25) M. Van Bavel, V. Leonov, R. F. Yazicioglu, T. Torfs, C. Van Hoof, N. E. Posthuma, and R. J. M. Vullers, *Sens. Transducers J.*, 2008, **94**, 103-115.
- (26) S. Ullah, H. Higgins, B. Braem, B. Latre, C. Blondia, I. Moerman, S. Saleem, Z. Rahman, and K. S. Kwak, *J. Medical Systems*, 2012, **36**, 1065-1094.
- (27) D. C. Hoang, Y. K. Tan, H. B. Chng, and S. K. Panda, *Proc. Int. Conf. Power Electronics and Drive Systems*, 2009, p. 1277-1282. (doi: 10.1109/PEDS.2009.5385814)
- (28) A. Dementyev, S. Hodges, S. Taylor, and J. Smith, *Proc. IEEE Int. Wireless Symposium*, 2013, p.1-4. (DOI: 10.1109/IEEE-IWS.2013.6616827)
- (29) H2: wearable blood pressure monitor, <http://www.h2care.com/>
- (30) J. H. Atkins, and J. E. Mandel, *Anesth. Analg.*, 2014, **119**, 1307-1314.
- (31) C. M. Lochner, Y. Khan, A. Pierre, and A. C. Arias, *Nat. Comm.*, 2014, **5**, 5745.

- (32) S. Ancoli-Israel, R. Cole, C. Alessi, M. Chambers, W. Moorcroft, and C. P. Pollak, *Sleep*, 2003, **26**, 342-392.
- (33) D. P. Rose, M. Ratterman, D. K. Griffin, L. Hou, N. Kelley-Loughnane, R. R. Naik, J. A. Hagen, I. Papautsky, and J. Heikenfeld, *IEEE Trans. Biomed. Eng.*, 2014, **62**, 1457-1465.
- (34) Y. Zhang, Y. Shakhsher, J. D. Silver, A. Klinefelter, M. Nagaraju, J. Boley, J. Pandey, A. Shrivastava, E. J. Carlson, A. Wood, B. H. Calhoun, and B. P. Otis, *IEEE J. Solid-State Circuits*, 2013, **48**, 199-213.
- (35) E. J. Carlson, K. Strunz, and B. P. Otis, *IEEE J. Solid-State Circuits*, 2010, **45**, 741-750.
- (36) C. Watkins, B. Shen, and R. Venkatasubramanian, *Proc. 24th Int. Conf. Thermoelectrics*, 2005, p. 265-267. (doi: 10.1109/ICT.2005.1519934)
- (37) A. P. Chandrakasan, D. C. Daly, J. Kwong, and Y. K. Ramadass, *Proc. IEEE Symposium on VLSI Circuits*, 2008, p. 2-5. (doi:10.1109/VLSIC.2008.4585930)
- (38) L. Mateu, C. Codrea, N. Lucas, M. Pollak, and P. Spies, *Proc. Int. Conf. Sensor Technologies and Applications*, 2007, p. 366-372. (doi: 10.1109/SENSORCOMM.2007.4394949)
- (39) J. Weber, K. Potje-Kamloth, F. Haase, P. Detemple, F. Völklein, and T. Doll, *Sensors and Actuators A*, 2006, **132**, 325-330.
- (40) A. Majumdar, *Science*, 2004, **303**, 777-778.
- (41) K. Biswas, J. He, I. D. Blum, C.-I. Wu, T. P. Hogan, D. N. Seidman, V. P. Dravid, and M. G. Kanatzidis, *Nature*, 2012, **489**, 414-418.
- (42) L.-D. Zhao, S.-H. Lo, Y. Zhang, H. Sun, G. Tan, C. Uher, C. Wolverton, V. P. Dravid, and M. G. Kanatzidis, *Nature*, 2014, **508**, 373-377.
- (43) J. Carrete, N. Mingo, S. Curtarolo, *Appl. Phys. Lett.*, 2014, **105**, 101907.

- (44) S. Sassi, C. Candolfi, J.-B. Vaney, V. Ohorodniichuk, P. Masschelein, A. Dauscher, and B. Lenoir, *Appl. Phys. Lett.*, 2014, **104**, 212105.
- (45) C.-L. Chen, H. Wang, Y.-Y. Chen, T. Day, and G. J. Snyder, *J. Mater. Chem. A*, 2014, **2**, 11171-11176.
- (46) G. S. Nolas, J. Poon, and M. Kanatzidis, *Mater. Res. Soc. Bull.*, 2006, **31**, 199-205.
- (47) G. J. Snyder, and E. S. Toberer, *Nat. Mater.*, 2008, **7**, 105-114.
- (48) B. Poudel, Q. Hao, Y. Ma, Y. Lan, A. Minnich, B. Yu, X. Yan, D. Wang, A. Muto, D. Vashaee, X. Chen, J. Liu, M. S. Dresselhaus, G. Chen, and Z. Ren, *Science*, 2008, **320**, 634-638.
- (49) X. Yan, B. Poudel, Y. Ma, W. S. Liu, G. Joshi, H. Wang, Y. Lan, D. Wang, G. Chen, and Z. Ren, *Nano Lett.*, 2010, **10**, 3373-3378.
- (50) R. Venkatasubramanian, E. Siivola, T. Colpitts, and B. O'Quinn, *Nature*, 2001, **413**, 597-602.
- (51) T. C. Harman, P. J. Taylor, M. P. Walsh, and B. E. LaForge, *Science*, 2002, **297**, 2229-2232.
- (52) C. J. Vineis, A. Shakouri, A. Majumdar, and M. G. Kanatzidis, *Adv. Mater.*, 2010, **22**, 3970-3980.
- (53) C. Brabec, U. Scherf, and V. Dyakonov ed., *Organic Photovoltaics: Materials, Device Physics, and Manufacturing Technologies* (Wiley-VCH Verlag, 2008).
- (54) Z. R. Li, *Organic Light-Emitting Materials and Devices*, 2nd ed. (CRC Press, Boca Raton, 2015)

- (55) R. Noriega, J. Rivnay, K. Vandewal, F. P. V. Koch, N. Stingelin, P. Smith, M. F. Toney, and A. Salleo, *Nat. Mater.*, 2013, **12**, 1038-1044.
- (56) A. Weathers, Z. U. Khan, R. Brooke, D. Evans, M. T. Pettes, J. W. Andreasen, X. Crispin, and L. Shi, *Adv. Mater.*, 2015, **27**, 2101-2106.
- (57) J. Liu, X. Wang, D. Li, N. E. Coates, R. A. Segalman, and D. G. Cahill, *Macromolecules*, 2015, **48**, 585-591.
- (58) C. Dames, in *Annual Review of Heat Transfer*, 2013, vol. 16, chap. 2, p. 7-49. (DOI: 10.1615/AnnualRevHeatTransfer.v16.20)
- (59) O. Bubnova, Z. U. Khan, H. Wang, S. Braun, D. Evans, M. Fabretto, P. Hojati-Talemi, D. Dagnelund, J.-B. Arlin, Y. H. Geerts, S. Desbief, D. Breiby, J. Andreasen, R. Lazzaroni, W. M. Chen, I. Zozoulenko, M. Fahlman, P. J. Murphy, M. Berggren and X. Crispin, *Nat. Mater.*, 2014, **13**, 190–194.
- (60) R. B. Aich, N. Blouin, A. Bouchard, and M. Leclerc, *Chem. Mater.*, 2009, **21**, 751-757.
- (61) C. Yu, K. Choi, L. Yin, and J. C. Grunlan, *ACS Nano*, 2011, **5**, 7885-7892.
- (62) M. Culebras, C. M. Gomez, and A. Cantarero, *J. Mater. Chem. A*, 2014, **2**, 10109-10115.
- (63) B. Zhang, J. Sun, H. E. Katz, F. Fang and R. L. Opila, *ACS Appl. Mater. Interfaces*, 2010, **2**, 3170–3178.
- (64) Z. H. Wang, K. Ichimura, M. S. Dresselhaus, G. Dresselhaus, W.-T. Lee, K. A. Wang, and P. C. Eklund, *Phys. Rev. B*, 1993, **48**, 10657-10660.
- (65) T. Menke, D. Ray, J. Meiss, K. Leo, and M. Riede, *Appl. Phys. Lett.*, 2012, **100**, 093304.
- (66) Y. Sun, P. Sheng, C. Di, F. Jiao, W. Xu, D. Qiu, and D. Zhu, *Adv. Mater.*, 2012, **24**, 932-937.

- (67) R. A. Schlitz, F. G. Brunetti, A. M. Glauddell, P. L. Miller, M. A. Brady, C. J. Takacs, C. J. Hawker, and M. L. Chabinyk, *Adv. Mater.*, 2014, **26**, 2825-2830.
- (68) S. L. Kim, K. Choi, A. Tazebay, and C. Yu, *ACS Nano*, 2014, **8**, 2377-2386.
- (69) K. Shi, F. Zhang, C.-A. Di, T.-W. Yan, Y. Zou, X. Zhou, D. Zhu, J.-Y. Wang, and J. Pei, *J. Am. Chem. Soc.*, 2015, published online. (DOI: 10.1021/jacs.5b00945)
- (70) C. Wan, X. Gu, F. Dang, T. Itoh, Y. Wang, H. Sasaki, M. Kondo, K. Koga, K. Yabuki, G. J. Snyder, R. Yang, and K. Koumoto, *Nat. Mater.*, 2015, **14**, 622-627.
- (71) J. H. We, S. J. Kim, G. S. Kim, and B. J. Cho, *J. Alloys Compd.*, 2013, **552**, 107-110.
- (72) S. J. Kim, J. H. We, J. S. Kim, G. S. Kim, and B. J. Cho, *J. Alloys, Compd.*, 2014, **582**, 177-180.
- (73) K. Yazawa, and A. Shakouri, *Environ. Sci. Technol.*, 2011, **45**, 7548-7553.
- (74) K. Yazawa and A. Shakouri, *J. Materials Research*, 2012, **27**, 1211-1217.
- (75) J. Sakamoto, J.-P. Fleurial, J. Snyder, S. Jones, and T. Caillat, *NASA Tech Briefs*, July 2006, NPO-40630.
- (76) K. Yazawa and A. Shakouri, *MRS Proceedings*, 2012, **1396**. (DOI: 10.1557/opl.2012.498)
- (77) J.-H. Bahk, K. Margatan, K. Yazawa, and A. Shakouri, *Advanced thermoelectric system simulator for waste heat recovery and energy harvesting*, <http://nanohub.org/tools/advte>.
- (78) V. Leonov, *Sensors Transducers J.*, 2011, **126**, 1-10.
- (79) V. Leonov, *J. Micromech. Microeng.*, 2011, **21**, 125013.
- (80) K. Yazawa and A. Shakouri, *J. Appl. Phys.*, 2012, **111**, 024509.
- (81) K. Yazawa and A. Shakouri, *J. Electron. Mater.*, 2012, **41**, 1845-1850.
- (82) C. Navone, M. Soulier, M. Plissonnier and A. L. Seiler, *J. Electron. Mater.*, 2010, **39**, 1755-1759.

- (83) R. R. Søndergaard, M. Hösel, N. Espinosa, M. Jørgensen and F. C. Krebs, *Energy Sci. Eng.*, 2013, **1**, 81-88.
- (84) N. Toshima, K. Oshima, H. Anno, T. Nishinaka, S. Ichikawa, A. Iwata and Y. Shiraishi, *Adv. Mater.*, 2015, **27**, 2246-2251.
- (85) J. H. We, S. J. Kim and B. J. Cho, *Energy*, 2014, **73**, 506-512.
- (86) Q. Wei, M. Mukaida, K. Kirihara, Y. Naitoh and T. Ishida, *RSC Adv.*, 2014, **4**, 28802-28806.
- (87) C. Zhuo, E. Koukharenko, M. J. Tudor, R. N. Torah and S. P. Beeby, *J. Phys.: Conference Ser.* 2013, **476**, 012031.
- (88) K. Suemori, S. Hoshino and T. Kamata, *Appl. Phys. Lett.* 2013, **103**, 153902.
- (89) Z. Cao, E. Koukharenko, R. N. Torah, J. Tudor and S. P. Beeby, *J. Phys.: Conference Ser.* 2014, **557**, 012016.
- (90) F. Jiao, C.-a. Di, Y. Sun, P. Sheng, W. Xu and D. Zhu, *Philos. Trans. R. Soc. A*, 2014, **372**, 20130008. (DOI: 10.1098/rsta.2013.0008)
- (91) Z. Lu, M. Layani, X. Zhao, L. P. Tan, T. Sun, S. Fan, Q. Yan, S. Magdassi and H. H. Hng, *Small*, 2014, **10**, 3551-3554.
- (92) E. Drahi, A. Gupta, S. Blayac, S. Saunier and P. Benaben, *Phys. Status Solidi A*, 2014, **211**, 1301-1307.
- (93) D. Madan, Z. Wang, A. Chen, R.-c. Juang, J. Keist, P. K. Wright and J. W. Evans, *ACS Appl. Mater. Interfaces*, 2012, **4**, 6117-6124.
- (94) D. Madan, Z. Wang, A. Chen, P. K. Wright and J. W. Evans, *ACS Appl. Mater. Interfaces*, 2013, **5**, 11872-11876.

- (95) D. Madan, Z. Wang, A. Chen, R. Winslow, P. K. Wright and J. W. Evans, *Appl. Phys. Lett.*, 2014, **104**, 013902.
- (96) S. E. Jo, M. K. Kim, M. S. Kim and Y. J. Kim, *Electron. Lett.*, 2012, **48**, 1013-1015.
- (97) P. Sheng, Y. Sun, F. Jiao, C. Di, W. Xu and D. Zhu, *Synth. Met.*, 2014, **193**, 1-7.
- (98) G. A. T. Sevilla, S. B. Inayat, J. P. Rojas, A. M. Hussain and M. M. Hussain, *Small*, 2013, **9**, 3916-3921.
- (99) M. A. Kamarudin, S. R. Sahamir, R. S. Datta, B. D. Long, M. F. Mohd Sabri and S. Mohd Said, *Sci. World J.*, 2013, **2013**, 17.
- (100) C. A. Hewitt, D. S. Montgomery, R. L. Barbalace, R. D. Carlson and D. L. Carroll, *J. Appl. Phys.*, 2014, **115**, 184502.
- (101) Y. Nonoguchi, K. Ohashi, R. Kanazawa, K. Ashiba, K. Hata, T. Nakagawa, C. Adachi, T. Tanase and T. Kawai, *Sci. Rep.*, 2013, **3**, 3344.
- (102) S. Baba, H. Sato, L. Huang, A. Uritani, R. Funahashi and J. Akedo, *J. Alloys Compd.*, 2014, **589**, 56-60.
- (103) K. Kato, Y. Hatasako, M. Kashiwagi, H. Hagino, C. Adachi and K. Miyazaki, *J. Electron. Mater.*, 2014, **43**, 1733-1739.
- (104) M. Mizoshiri, M. Mikami and K. Ozaki, *Jpn J. Appl. Phys.*, 2013, **52**, 06GL07.

Figure captions

FIG. 1. Three types of wearable sensor nodes powered by thermoelectric energy harvesters. The thermoelectric generators are preferably made of flexible materials and substrates, so that they can be conformally attached on the various locations of the skin with enhanced thermal contact. Monitored data are transmitted via a short-distance wireless communication protocol such as Bluetooth, ANT, or Zigbee to a portable personal server such as a cell phone, and then to the remote healthcare service provider via a long-distance network.

FIG. 2. (a) Electrical conductivity, (b) Seebeck coefficient, and (c) power factor of selected key flexible thermoelectric materials, both p-type (left) and n-type (right), measured at room temperature. Properties of bulk Bi_2Te_3 alloys are also shown for comparison. Numbers in brackets are references.

FIG. 3. (a) Schematic of a thermoelectric energy harvester, and (b) the thermal and electric circuit models used for device performance simulation. Symbol ψ denotes a thermal resistance, and R denotes an electrical resistance.

FIG. 4. Calculated (a) voltage output and (b) power output for the inorganic-polymer hybrid material (the first row in Table 1), and similarly, (c) voltage output and (d) power output for the screen-printed inorganic material (the second row in Table 1). Module size is $3 \text{ cm} \times 15 \text{ cm}$ (wrist-band type), and the cross-sectional area of each TE element is $0.5 \times 0.5 \text{ cm}^2$. The number of TE elements was determined by the fill factor. The thermal conductivity of the gap filler is

$0.03 \text{ W m}^{-1} \text{ K}^{-1}$. Note that these results are calculated for a fixed module size ($3 \text{ cm} \times 15 \text{ cm}$), but in principle both voltage and power outputs increase proportionally with module size.

FIG. 5. Power output with varying gap filler thermal conductivity for the inorganic-polymer hybrid material (first row in Table 1) as a function of TE element thickness. The fill factor was fixed to 0.1.

Tables

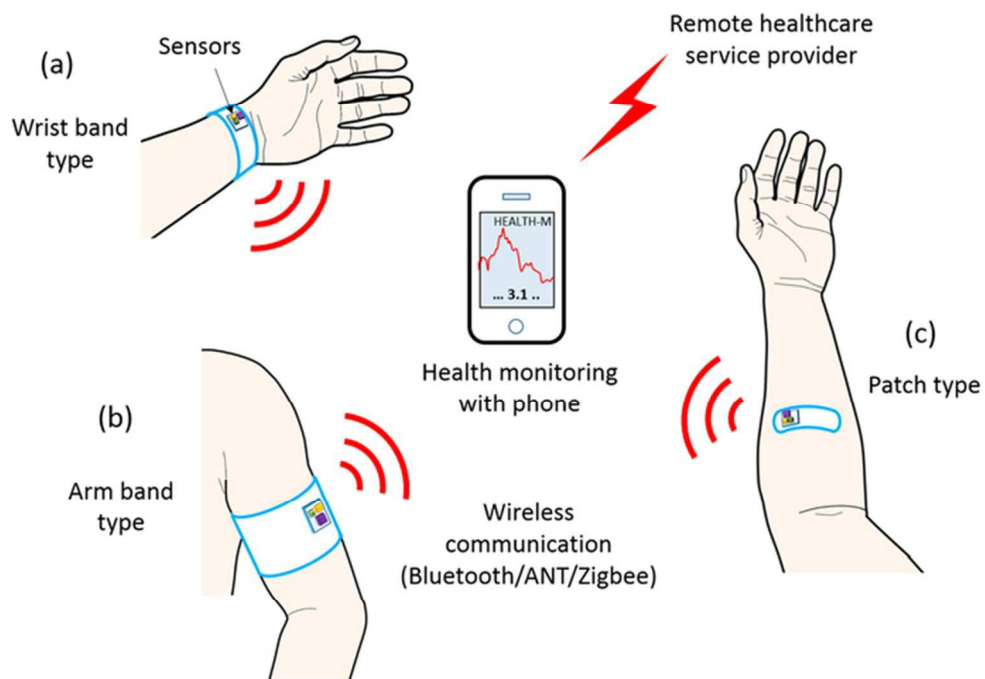
Table 1. Two sets of room temperature material properties used for device simulations. The inorganic-polymer hybrid is based on the data from Zhang et al.[63] for PEDOT:PSS on Bi₂Te₃ film, and the screen-printed inorganic is based on the data from Kim et al.[21].

Material type		σ (S cm ⁻¹)	S (μ V K ⁻¹)	$S^2\sigma$ (μ W m ⁻¹ K ⁻²)	κ (W m ⁻¹ K ⁻¹)	ZT
Inorganic-polymer hybrid	p-type	60	150	135	0.3	0.135
	n-type	60	-120	86	0.3	0.086
Screen-printed inorganic	p-type	1300	95	1170	1.3	0.27
	n-type	600	-140	1180	1.0	0.35

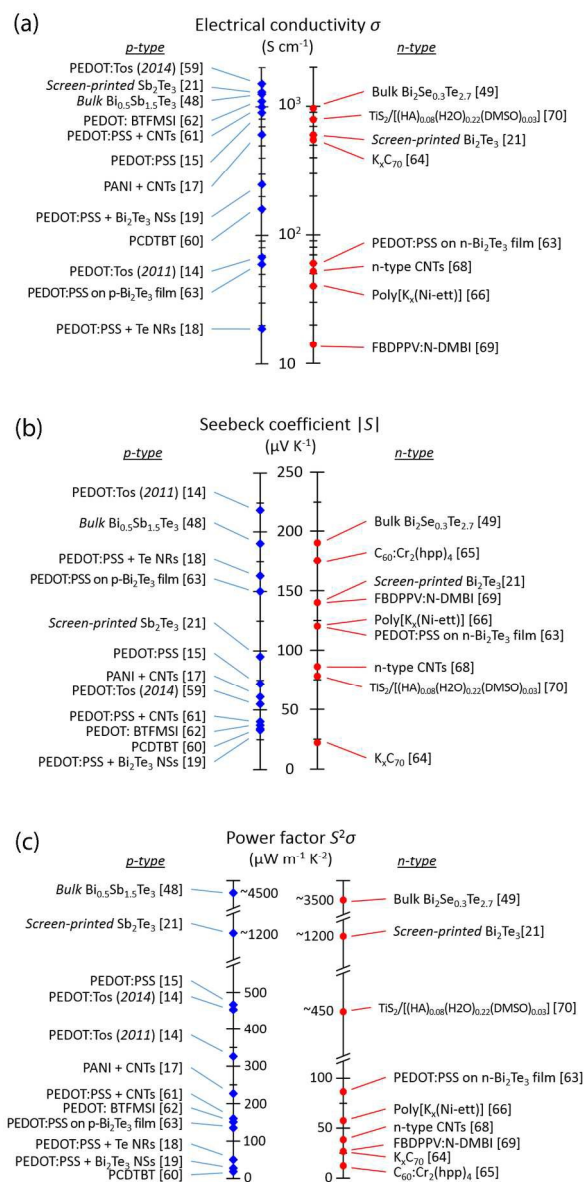
Table 2. A summary of materials and experimental performance results of flexible TEGs grouped by their fabrication methods.

Methods	Materials		D_{film} (μm)	R_{in} (Ω)	ΔT (K)	N	V_{oc} (mV)	P_{max} (μW)	Ref.
	p-type	n-type							
Screen printing	$\text{Sb}_2\text{Te}_3/\text{epoxy}$	$\text{Bi}_2\text{Te}_3/\text{epoxy}$	500	<1	50	8	90	10.5	[21]*
	PEDOT:PSS	-	1.3	138	65	567	0.18	5.5e-5	[83]*
	-	CNT composite	0.1	26	100	5	20	4	[84]
	$\text{Sb}_2\text{Te}_3/\text{PEDOT:PS}$	$\text{Bi}_2\text{Te}_3/\text{PEDOT:PSS}$	40	145	50	7	85	12	[85]
	PEDOT:PSS	-	20	10	100	300	40	50	[86]
	$\text{Sb}_2\text{Te}_3/\text{epoxy}$	$\text{Bi}_2\text{Te}_3/\text{epoxy}$	65	800	20	4	25	0.19	[87]
	CNT/polystyrene	-	150	352	70	198	305	66	[88]*
	$\text{Sb}_2\text{Te}_3/\text{epoxy}$	$\text{Bi}_2\text{Te}_3/\text{epoxy}$	60	7200	20	8	36	0.04	[89]
Inkjet printing	$\text{Sb}_2\text{Te}_3/\text{epoxy}$	$\text{Bi}_2\text{Te}_3/\text{epoxy}$	500	300	30	20	25	2	[20]*
	poly[$\text{Cu}_x(\text{Cu-ett})$]/PVDF	poly[$\text{K}_x(\text{Ni-ett})$]/PVDF	3	54	25	6	15	1	[90]
	-	$\text{Bi}_2\text{Te}_{3-x}\text{Se}_x/\text{epoxy}$	120	480	20	62	220	25	[93]
	$\text{Bi}_{0.5}\text{Sb}_{1.5}\text{Te}_3/\text{epoxy}$	-	120	800	20	60	270	21	[94]
	$\text{Bi}_{0.5}\text{Sb}_{1.5}\text{Te}_3/\text{epoxy}$	Bi/epoxy	120	100	70	10	210	130	[95]
Molding	$\text{Bi}_{0.5}\text{Sb}_{1.5}\text{Te}_3/\text{epoxy}$	$\text{Bi}_2\text{Te}_{3-x}\text{Se}_x/\text{epoxy}$	4000	170	25	15	35	5	[96]*
	Cu(I)-ett	poly[$\text{K}_x(\text{Ni-ett})$]	5000	557	60	220	1510	1000	[97]*
lithography	PEDOT:Tos	TTF-TCNQ	30	-	10	54	-	0.13	[14]*
	Sb_2Te_3	Bi_2Te_3	0.7	2400	20	63	37	0.14	[98]
CNT composites	CNT	CNT/PEI	-	16000	50	45	21	0.66	[100]
	CNT/SDBS	CNT/PEI	8	12000	50	72	460	4.4	[68]
	CNT/tpp	CNT/TCNQ	80	82	20	3	6	0.11	[101]
Vacuum deposition	$(\text{Bi}_{0.15}\text{Sb}_{0.85})_2\text{Te}_3$	-	200	77	34	24	130	55	[102]
	$\text{Bi}_{0.4}\text{Sb}_{1.6}\text{Te}_3$	$\text{Bi}_2\text{Te}_{2.7}\text{Se}_{0.3}$	1	1200	130	18	600	100	[103]
	Sb_2Te_3	Bi_2Te_3	16	8300	20	10	42	5.3e-2	[104]

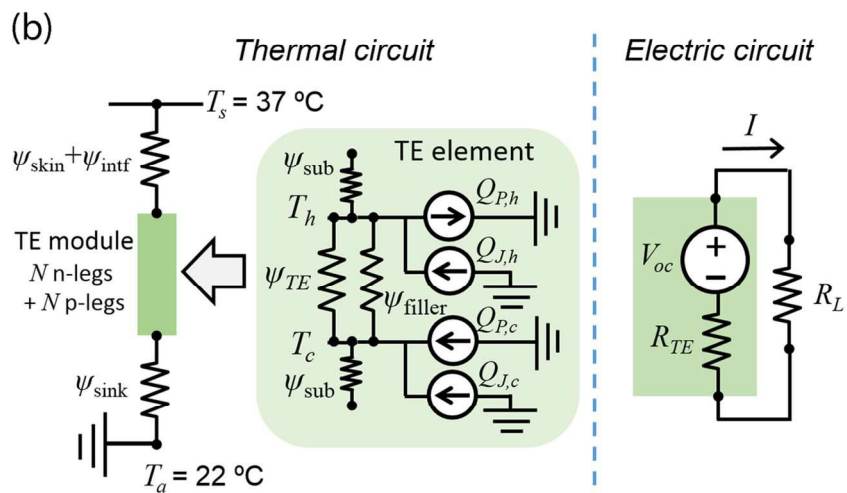
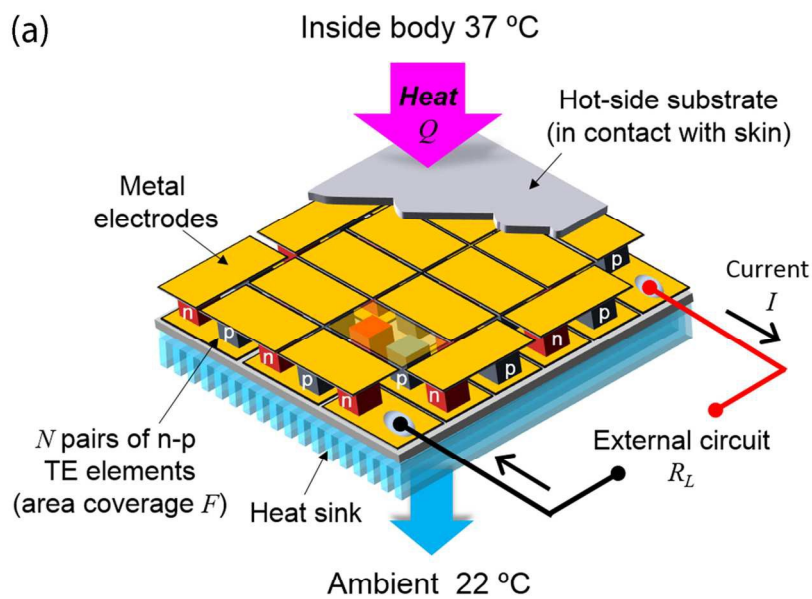
D_{film} , R_{in} , ΔT , n , V_{oc} and P_{max} stand for, respectively, thickness of each element, total internal resistance of the TEG, temperature difference (the highest achieved), number of TE element pairs, open circuit voltage, and maximum power output with matching load resistance. In the references marked with *, the temperature gradient is in the cross-plane direction; otherwise, it is in the in-plane direction. In the Materials columns, PVDF is poly(vinylidene fluoride), TTF-TCNQ is tetrathiafulvalene-tetracyanoquinodimethane, SDBS is sodium dodecylbenzenesulfonate, and tpp is triphenylphosphine.



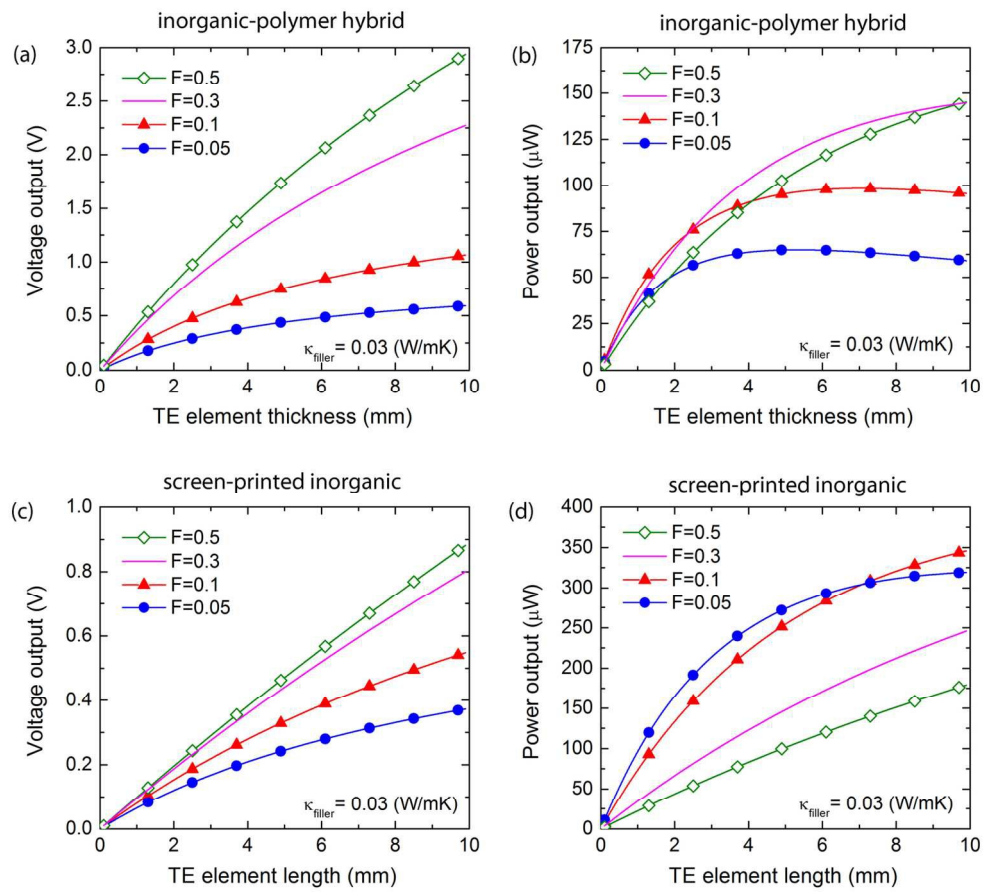
60x41mm (300 x 300 DPI)



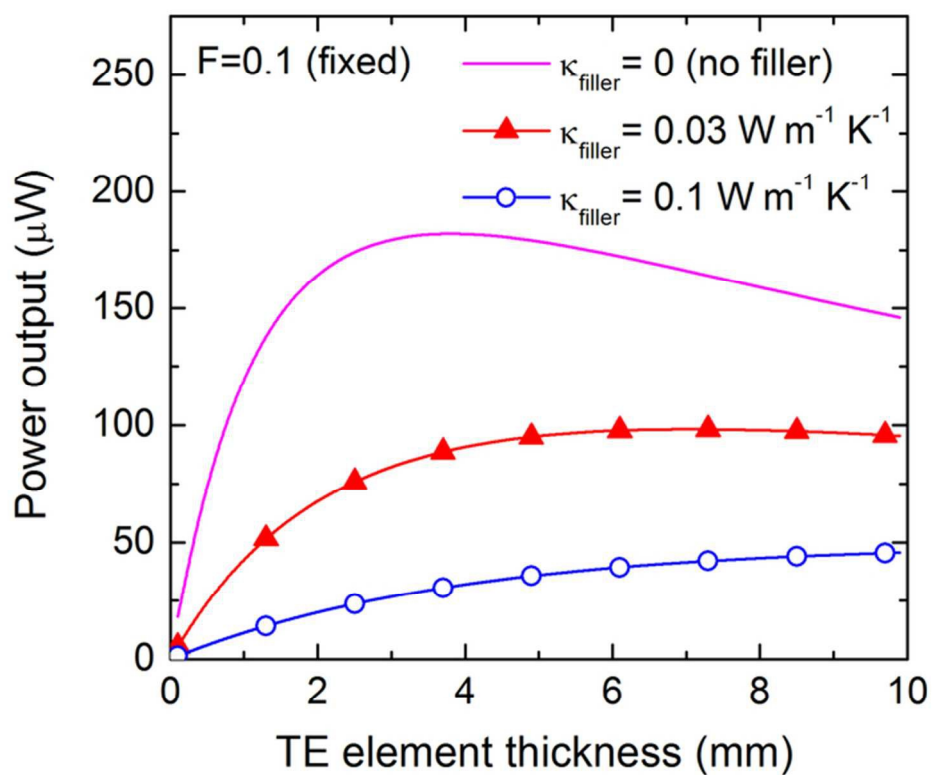
167x345mm (300 x 300 DPI)



110x150mm (300 x 300 DPI)



139x128mm (300 x 300 DPI)



63x52mm (300 x 300 DPI)